

# Wide-angle Micro Sensors for Vision on a Tight Budget

Sanjeev J. Koppal\*  
Harvard University

Ioannis Gkioulekas\*  
Harvard University

Todd Zickler\*  
Harvard University

Geoffrey L. Barrows†  
Centeye, Inc.

## Abstract

Achieving computer vision on micro-scale devices is a challenge. On these platforms, the power and mass constraints are severe enough for even the most common computations (matrix manipulations, convolution, etc.) to be difficult. This paper proposes and analyzes a class of miniature vision sensors that can help overcome these constraints. These sensors reduce power requirements through template-based optical convolution, and they enable a wide field-of-view within a small form through a novel optical design. We describe the trade-offs between the field of view, volume, and mass of these sensors and we provide analytic tools to navigate the design space. We also demonstrate milli-scale prototypes for computer vision tasks such as locating edges, tracking targets, and detecting faces.

## 1. Introduction

The recent availability of portable camera-equipped computers, such as smart-phones, has created a surge of interest in computer vision tools that can run within limited power and mass budgets. For these platforms, the focus has been to create optimized hardware and software to analyze conventional images in a highly efficient manner. Yet, there is a class of platforms that are *still smaller*. These are micro-platforms (characteristic size  $< 1\text{mm}$ ) that have power and mass constraints severe enough for large-scale matrix manipulations, convolution, and other core computations to be impossible. These platforms appear in many domains, including micro-robots and other small machines [8], and nodes of far-flung sensor networks [32].

Power is the critical issue when shrinking a vision system to the micro scale, with many platforms having average power budgets on the order of milli-Watts. In this paper, we present and analyze a class of micro vision sensors that can help overcome the constraints of low power. Arrays of these sensors could handle a specific vision task, like face detection, as depicted in Fig. 1.

A wide field-of-view (FOV) is important for saving power, since low-FOV devices must either pan a single sensor or carry multiple sensors with different viewpoints. Our designs obtain a large FOV within a small form by exploit-

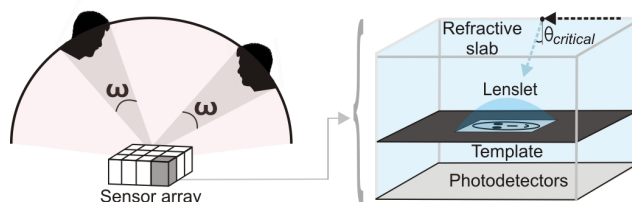


Figure 1. We propose a miniaturized class of wide-angle sensors. Arrays of these sensors handle specific tasks. A refractive slab creates a  $180^\circ$  field-of-view due to Snell’s law. Attenuating templates in the viewing path allow optical filtering and enable vision tasks such as locating edges, tracking targets and detecting faces.

ing the “Snell’s window” effect [10, 43]. This effect, which we induce with refractive slabs, is observed by underwater divers who can see a  $180^\circ$  FOV of the outside world because grazing incident light rays are refracted at the water-air boundary by the critical angle.

Our designs also lower power consumption by reducing on-board computation. Template-based filtering, an expensive component of many vision algorithms, is usually computed as a post-capture operation in hardware or software. Instead, we place attenuating templates in the optical path, allowing our sensors to perform filtering, “for free”, prior to image capture. In conventional two-dimensional image filtering, sliding templates are applied with fixed spatial support over the image plane. Similarly, our designs ensure that the template’s *angular support*, given by the solid angle  $\omega$  in Fig. 1, is near-constant over the hemispherical visual field. In this sense, we extend well-known planar optical filtering mechanisms [45, 28] to the wide FOV case, by ensuring consistent template responses across view directions.

Our optical designs offer a new approach to efficiently implement vision algorithms on micro-platforms. However, this efficiency comes at a cost, which is the penalty exacted by the mass and volume of the optics. The main contribution of this paper is a description and formalization of the fundamental trade-offs that exist between field of view, filtering accuracy, volume, and mass of these sensors, which subsume a variety of optical configurations, including lensless apertures, lenslets, and refracting slabs. We present solutions for the parameters that widen the field of view while minimizing sensor size, and we validate these equations empirically. In addition, as applications of this theory, we demonstrate milli-scale prototypes that are designed for edge detection, target tracking, and face detection.

\* (sjkoppal, igkiou, zickler)@seas.harvard.edu

† geof@centeye.com



## 4. Analysis

Our goal is to analyze the class of sensing elements shown in Fig. 2, formalizing the tradeoffs between the effective field of view and the element’s volume and mass. A single sensor’s design parameters form a five dimensional vector  $\Pi = \{u, d, n_1, n_2, R\}$ , where  $u$  is the template height,  $d$  is the template width,  $n_1$  is the medium’s refractive index,  $n_2$  is the lenslet’s refractive index, and  $R$  is its radius of curvature. Choosing a set of design parameters  $\Pi$  determines the angular support measured in each view direction  $\theta$ , and we represent this as a scalar angular support function,  $\omega(\theta; \Pi)$ . For convenience, we shorten this function to  $\omega(\theta)$ , or  $\omega(x)$ , since there is a one-to-one mapping between viewing angle  $\theta$  and photodetector coordinate  $x$ .

We define the effective field of view (eFOV) to be the set of view directions for which the angular support is sufficiently close to a constant, desired angular support  $\omega_o$ . Formally, we write this as  $|\Theta|$  with  $\Theta = \{\theta : F(\omega(\theta; \Pi), \omega_o) \leq \Delta\}$ , where  $\Delta$  is a user-defined threshold, and  $F(\omega(\theta; \Pi), \omega_o)$  is some distance metric. We will assume  $\Theta$  includes the optical axis ( $\theta = \frac{\pi}{2}$ ), and we use the  $L_2$  distance metric, so that  $F(\omega, \omega_o) = \|\omega - \omega_o\|_2$ .

While templates can be fabricated by a variety of processes, there will be limits to the achievable spatial resolution and, equivalently, the minimum “dot pitch”. This gets translated, through our optics, into an angular resolution over the support  $\omega$ . For a particular setup, there will be a minimum angular resolution that can be tolerated and we represent this as the corresponding *angular dot pitch*  $d\omega$ .

Suppose we wish to implement a particular filtering operator, which is optically defined by the design specifications  $\Xi = \{\omega_o, \Delta, d\omega, F\}$ . Let the first element of  $\Xi$  be  $10^\circ$ ; this means that our design should have a near-constant angular support of  $\omega \approx 10^\circ$  over a wide field of view. If there exists a family of design parameters  $\Pi$  that can achieve this goal, how do we find “good” members of this family? Of course, depending on the application and the platform, the “best” design could be one with minimum volume or mass (or both), or one that provides the maximum possible eFOV or perhaps the maximum eFOV under some size constraints.

The main contribution of this section is to derive equations and present empirical analysis, in the form of a look-up table, to answer all these types of questions, and allow designing a custom sensor. For all cases, we show experimental validation, summarized in Fig. 5.

Note that the design parameters  $\Pi$  are limited by a number of constraints  $\Psi$ , of which there are two classes:

- The design parameters  $\Pi$  must be *physically plausible*, with  $u, d, R \geq 0$ ,  $n_1, n_2 \geq 1$ ,  $d \leq 2R$  (from the lens equation) and  $n_2 \geq n_1$  (to create a convex lens).
- The design parameters  $\Pi$  must allow *easy micro-fabrication*. Diffraction effects [26] place a strict lower

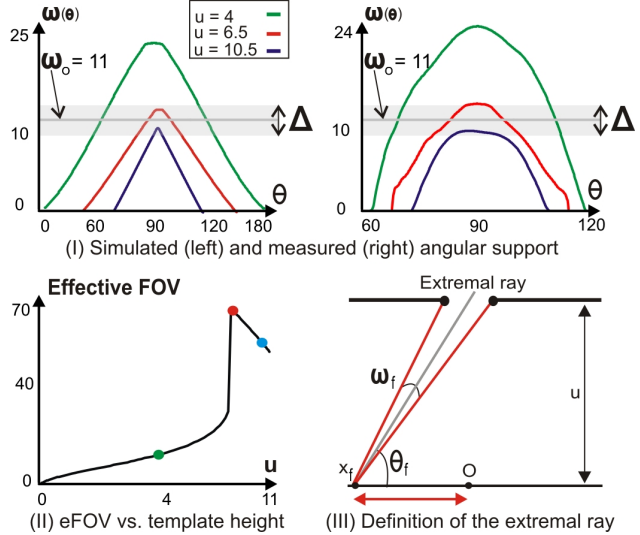


Figure 3. **Optimal lensless parameters:** I shows measured and simulated solid angles for three template heights  $u$  for a  $d = 0.1$ mm pinhole. The measured angles compare well to simulations. The maximum eFOV occurs at an optimal  $u$  peak in II.

bound on our ability to shrink the designs, but in practice, three issues emerge earlier: the minimum template width  $d_{min}$  for which the template printing process can still achieve the desired angular dot pitch  $d\omega$ ; the maximum photodetector array length  $E_{max}$ , which may be fixed or custom built; and  $t$ , the aperture thickness, shown in Fig. 2, whose vignetting effect on angular support is explained in the Appendix.

### 4.1. Designs without Snell’s window

Consider a **lensless** version of Fig. 2 where the refractive indices  $n_1 = n_2 = 1$  imply that both the internal angular supports,  $\omega'$  and  $\omega''$ , are equal to the external angular support  $\omega$ . Therefore the design parameter space is two-dimensional,  $\Pi = \{u, d\}$ . Fig. 3(I) shows angular support curves  $\omega(\theta)$  for a fixed template width  $d = 0.1$ mm and three different template heights  $u = \{4, 6.5, 10.5\}$ . These curves were measured using our prototype, shown in Fig. 7 (I).

This figure shows how the angular support function undergoes approximate vertical shifts as the template height  $u$  varies. The central curve, which is tangential to the upper bound  $\omega_o + \frac{\Delta}{2}$ , is most desirable because it provides the largest eFOV. Since mass is negligible for this design, we can define an “optimal design  $\Pi^{**}$ ” as the one that achieves this largest possible eFOV while fitting within the smallest possible volume, given the constraints  $\Psi$ .

We will find this optimal design in three steps: (1) randomly select a large value for template width  $d$ ; (2) find a template height  $u$  such that the  $(u, d)$  pair has maximal eFOV; and (3) globally scale down the design till we reach a constraint in  $\Psi$ . In our discussion, we will consider only the constraint of minimum template width  $d_{min}$ , but the same

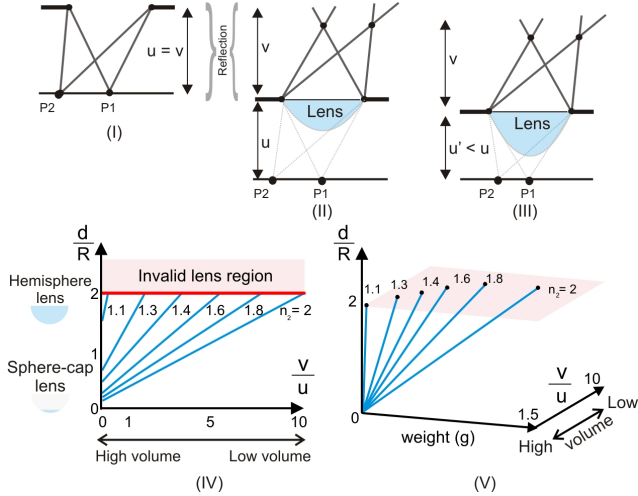


Figure 4. **Volume-Weight tradeoffs for lenslets in air:** The ray geometry in (I) is identical to the unrefracted, incident rays in (II). The design in (III) is heavier than that in (II), but requires a smaller volume ( $u' < u$ ). While there exists an advantage in volume (IV) gained by increasing the refractive index, (V) shows the cost in weight that must be paid to achieve this compression. Note that valid thin lenses must have  $d \leq 2R$ .

procedure can be used directly for others. Finally, we define  $x_f$  as the extreme point furthest from the origin  $O$  for which  $\omega(x_f) \in [\omega_o - \frac{\Delta}{2}, \omega_o + \frac{\Delta}{2}]$ . We also define  $\theta_f$  to be the corresponding extreme view, as in Fig. 3 (III).

This two-step algorithm is supported by the fact that there exists only a one-dimensional family of maximal eFOV solutions for the design parameters  $\Pi$  in the lensless case. Recall that the eFOV depends only on angular quantities (angular support  $\omega$ , viewing direction  $\theta$ ), which remain unchanged with global linear scaling of the lengths and distances in Fig. 2. Therefore there exists at least a one-dimensional family of lensless design parameters,  $\Pi_k = \{ku, kd\}$ , parameterized by scale  $k$ , which have identical eFOV. To show that this is the only family of solutions, let us suppose there existed design parameters  $\Pi' = \{u', d'\}$  outside the design parameter family  $\Pi_k$  but with identical eFOV. Consider a value of  $k = \frac{u}{u'}$  such that the design parameters  $\Pi_k$  and  $\Pi'$  have the same photo-detector distance  $u$  but still different template widths  $d \neq \frac{u}{u'} d'$ . Now consider the extreme viewing angle  $\theta_f$  (Fig. 5 (III)) of the design parameters  $\Pi'$ . This last photodetector element  $x_f$  integrates the angular support  $\omega_f$  such that  $\omega_f = \omega_o - \frac{\Delta}{2}$ . The expression for any angular support is  $\omega = \arccos\left(\frac{2u^2 + 2x^2 - \frac{d^2}{2}}{2\sqrt{(u^2 + (\frac{d}{2} - x)^2)(u^2 + (\frac{d}{2} + x)^2)}}\right)$ , from the geometry of Fig. 2. This implies templates of different widths subtending angles from the same height  $u$  at the same coordinate  $x_f$  must subtend different angles. Therefore, the angular support at  $x_f$  cannot equal  $\omega_f$  in the design parameter  $\Pi_k$ , and the design parameters  $\Pi'$  are in the family.

Returning to step (1) of our algorithm, we first guess a large positive value for the template width  $d$ . In step (2), we know definitely that a value of the template height  $u$  exists with maximal eFOV, since the family of design parameter solutions is  $\Pi_k$ . Intuitively, this maximal eFOV occurs when the curve in Fig. 3 (I) “kisses” the threshold  $\Delta$ ’s boundary, such that the origin’s angular support is  $\omega_o + \frac{\Delta}{2}$ .

We use a simple grid search to find the optimal template height  $u$ , but empirical evidence (Fig. 3 (II)) suggests that gradient-based methods may prove effective. Finally, in step (3), once we have a maximal eFOV candidate, we scale the design parameters  $\Pi$  downwards to obtain  $k_{min}$ , such that any further reduction would violate the minimum template width  $d \geq d_{min}$ .

For a **lenslet in air**, both internal angular supports are different while one is equal to the external angular support,  $\omega = \omega' \neq \omega''$ . The lenslet’s refractive index is higher than the surrounding medium (air),  $n_2 > n_1 = 1$ , and therefore the design parameters are  $\Pi = \{u, d, n_2, R\}$ . We propose a two-step method to obtain the design parameters  $\Pi$ : 1) find a corresponding lensless design  $\Pi_l = \{u_l, d_l\}$ ; and 2) trade-off volume and weight using lenslet parameters ( $n_2, R$ ).

In step (1), we start with a simple geometric argument, illustrated in Fig. 4 (I-II). The figure shows that, for any lenslet (II), there exists a lensless ray geometry (I) which is the same (under a mirror reflection) to the exterior, unrefracted rays in (II). Fig. 5(II) shows simulated and measured angular support curves  $\omega(\theta)$  for a 3mm lenslet, which are similar to the lensless case. Therefore we first perform step (1) and find design parameters  $\Pi_l = \{d_l, u_l\}$ , as done in the previous lensless section. We convert this into an initial lenslet design by selecting a random refractive index  $n_2 > 1$  and a valid lens  $R$ .

In step (2), the design parameters  $\Pi$  can be modified according to a two-dimensional volume-weight tradeoff by either increasing the lenslet refractive index  $n_2$  or decreasing the radius of curvature  $R$ , illustrated in Fig. 4 for a desired angular support of  $\omega_o = 16^\circ$ . Note that a downward lens orientation in Fig. 4(II-III) is helpful in allowing us to decrease the template height  $u$  without adding new volume to the design. This is physically possible if the lenslet refractive index  $n_2 \leq 2$ , which forces the radius to be less than both the focal length and template height  $R \leq f < u$ .

Increasing the lenslet refractive index  $n_2$  or decreasing the radius  $R$  makes the design heavier, but enables a shorter focal length. This allows a smaller assembly with no change in eFOV. The graphs in Fig. 4 (IV) are the volume reductions provided by different refractive indices. The best compression is achieved where these lines intersect the  $d \leq 2R$  constraint in  $\Psi$ . However, Fig. 4 (V) shows the weight increases as the volume decreases, suggesting that the “best” choice is a design decision, unlike the lensless case.

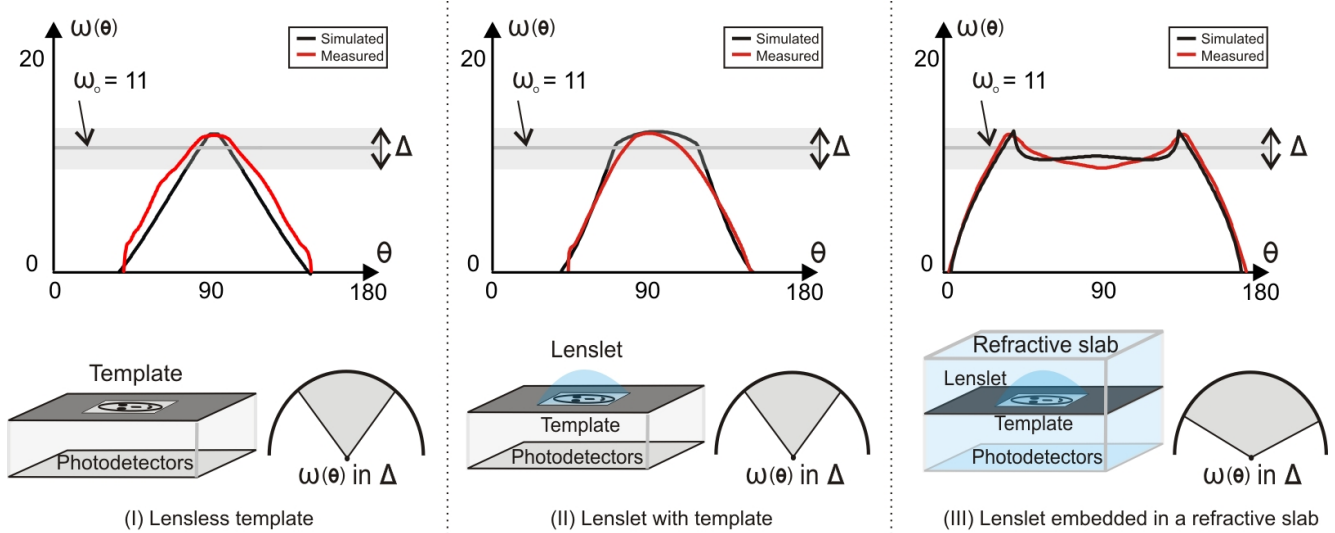


Figure 5. Simulated and measured angular support graphs for lensless sensors, lenslets in air and embedded lenslet sensors. The fields of view are given by the set of angles  $\theta$  for which  $\omega(\theta) \in \omega_o \pm \frac{\Delta}{2}$ . Below each graph are drawings of the design and the eFOV. Note the high eFOV of the embedded lens with the Snell’s window effect.

## 4.2. Designs with Snell’s window

To achieve a greater eFOV, we require an embedding medium. Figure 5 (III) shows an example of the Snell’s window effect on the external angular support  $\omega$ , which remains within the user-defined threshold  $\Delta$  for a much larger set of viewing angles than for the non-embedded cases.

We provide an empirical overview of the design parameters  $\Pi = \{u, d, n_2, n_1, R\}$  for lenslets embedded in a medium, and build a look-up table for designers wishing to constrain or specify the desired weight, volume and eFOV characteristics of a sensor. We take advantage of the small sensor sizes and assume reasonable ranges on the values of  $u$ ,  $d$  and  $R$ . For every set of design parameters  $\Pi$ , within this range, we find the eFOV in a brute force manner, taking into account the change in effective lenslet focal length due to the embedding [31].

The sensor’s volume, given by the design parameters  $\Pi$ , is computed as  $V = 2x_f u$ , while its weight is given by  $W = V_l \rho_2 + (V - V_l) \rho_1$ , where  $V_l$  is the volume of the lenslet, computed as a spherical cap, and  $\rho_1$  and  $\rho_2$  are the densities of the refractive indices  $n_1$  and  $n_2$ . We obtain these by assuming a linear relationship between optical and physical densities [13].

Figure 6 visualizes the lookup table for a desired angular support of  $\omega_o = 12^\circ$  and a user defined threshold  $\Delta = 2.4^\circ$  by projecting it onto the (volume, weight) plane. Each point in the plane shows the maximal eFOV of all sampled design parameters  $\Pi$ s at that point. Not every set of parameters  $\Pi$  was sampled, and designs that were not included create black spacings. On the right, we color code

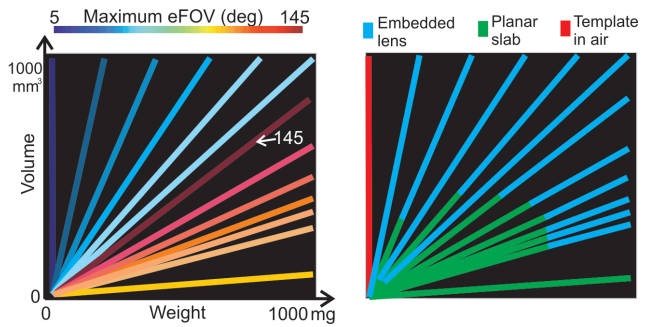


Figure 6. **Volume-Weight lookup table for  $\omega_o = 12^\circ$** : Here we project the (Volume, Weight, eFOV) look-up table onto the Volume-Weight plane, by only plotting the maximal eFOV at each plane coordinate. Note that design parameters  $\Pi$ s with the same eFOV form one-dimensional spaces (lines). However, more than one configuration can create the same eFOV, as shown by the masks on the right, which color-code the optical designs. The design variations in this figure are best viewed in color.

the graph according to the class of optical design. The figure clearly shows lines with the same eFOV. This is because, given any set of design parameters  $\Pi$ , we can generate a family of designs with equivalent eFOV through  $\Pi_k = \{ku, kd, n_2, n_1, kR\}$ . However, unlike in previous discussions, there may exist other optical designs, outside this one-dimensional space, that have the same eFOV. This is depicted by the color transitions in some lines. Reddish hues depict higher eFOV, and it is not surprising that many of these slope toward higher weight, implying refractive optics are used. The red vertical lensless design is likely to be only useful when zero weight is essential. Finally, there is no “best” design, since the maximum eFOV of  $145^\circ$  is neither very low in volume nor in weight.

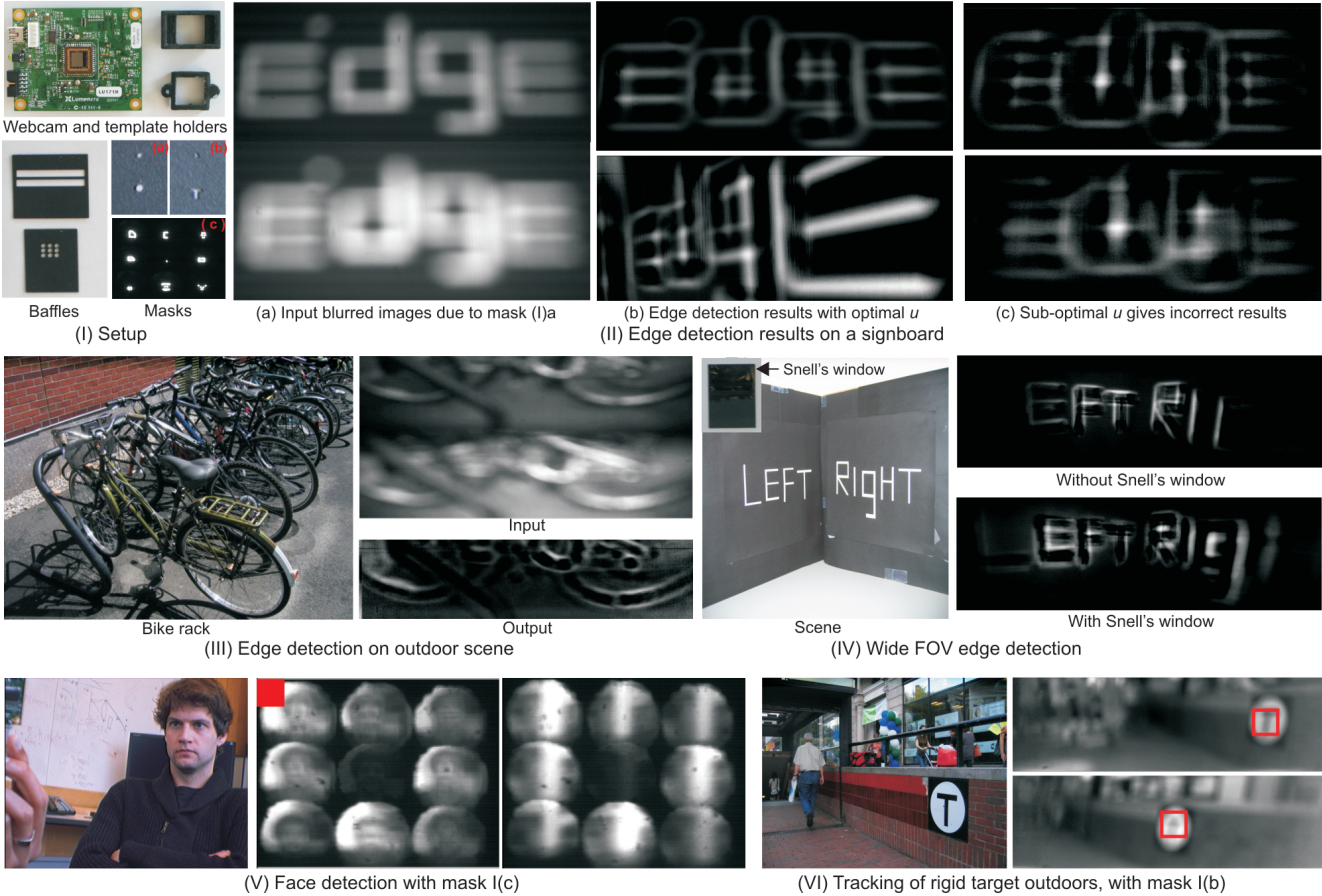


Figure 7. **Applications:** In (I) we show our setup: a camera with custom template holders. We use template I(a) to obtain two blurred versions of the scene, as in II(a). This allows edge detection through simple subtraction as in II and III. Without our optimal parameters, the edge detection is unreliable II(c). Wide-FOV edge detection is possible with a Snell’s window enhanced template shown in (IV). In (V), mask I(c) was learnt from a face database [22], and the nine mask responses are used by a linear classifier to provide face detection. In (VI) we show rigid target tracking using mask I(b), which includes two templates.

## 5. Experiments and Applications

The ability to provide a wide eFOV for optical convolution allows us to miniaturize previously proposed template-based vision techniques. In Fig. 7 (I) we show our prototype, which consists of a camera (Lu-171, Lumenera Inc.) with custom 3D-printed template assembly. We either cut binary templates into black card paper using a 100-micron laser (VLS3.50, Versa Inc.) or have grayscale patterns printed on photographic film (PageWorks Inc., <http://www.pageworks.com/>). We divide the camera photodetector plane into multiple single-template sensor elements using opaque baffles that are created from layered paper to prevent cross-talk between the sensor elements. Snell’s window is achieved by attaching laser-cut pieces of acrylic (refractive index  $n_1 = 1.5$ ) to the templates. UV cured optical glue of the same refractive index is used to bind these and fill the air gaps in the templates.

Before we describe the applications in Fig. 7, we show some experimental validation related to the previous sec-

tion. Recall that many design parameters (II) may exist with the same eFOV, while differing in volume, mass and other characteristics. Fig. 8(I) shows three such sensor measurements of a face. The first is taken with a lensless configuration with a large template height  $\{d = 2.5\text{mm}, u = 70\text{mm}\}$ , the second with a reduced template width  $\{d = 0.1\text{mm}, u = 2.8\text{mm}\}$  and the third with an embedded lenslet configuration  $\{d = 2.5\text{mm}, R = 2.12\text{mm}, n_2=1.85, n_1 = 1.5, u = 12\text{mm}\}$ . An obvious lens advantage is that it collects more light, hence, the third measurement has better SNR than the second. A more subtle issue is that the second sensor’s volume is smaller than the first, even though the measurement quality appears similar. We now demonstrate three vision applications of our sensors:

**Locating edges:** A classical approach to edge detection at a particular scale is to convolve an image with a Laplacian of Gaussian filter [25]. This is often approximated by a difference-of-Gaussians, and we can do the same here by convolving the scene with two radially-symmetric filters, in the optical domain. Such a sensor would obtain two dif-

ferently blurred scene measurements, and compute an edge map simply by subtracting corresponding pixels. While the computational savings of this approach are negligible when computing fine scale edges (low width Gaussians), they increase as the desired edges become more coarse, or if the elements are tiled for multi-scale edge detection (e.g., [11]).

Fig. 7(II) demonstrates this using two disk-shaped binary templates of different radii. Like a difference-of-Gaussian operator, differences between corresponding pixels in the two sensor elements produces a band-limited view of the scene (an edge map). This is a lensless configuration with two templates with the same heights,  $\{d = 0.1\text{mm}; u = 3.7\text{mm}\}$  and  $\{d = 0.2\text{mm}; u = 3.7\text{mm}\}$  with a (maximized) eFOV of  $90^\circ$ . The figure shows edges of a simple scene with printed words. A naive use of the sensors with suboptimal  $u$  values of 2mm and 5mm produces incorrect results. Fig. 7(III) shows results with an outdoor scene of a bike stand, while Fig. 7(IV) shows a V-shaped scene viewed by a simple pinhole and by a wide-FOV Snell’s window enhanced sensor, which can “see” more letter edges.

**Detecting faces:** Face detection in the traditional post-capture processing sense can be formulated as a two-step process in which: 1) the image is convolved with a series of templates, and 2) the template responses at each pixel are used as input to a binary classifier. In the past, efficiency has been gained by using “weak” but computationally convenient templates in relatively large numbers [39]. By performing the filtering step optically, we reduce the computational cost further, and since we can use templates with arbitrary spatial patterns and spectral selectivity, we can potentially reduce the number of templates substantially.

Optimized spatio-spectral templates can surely be learned for discriminating between faces and background, but we leave this for future work. Instead, in Fig. 7(V) we demonstrate a simple prototype that used nine *binary templates* learned using a subset of the PubFig Database [22] as positive examples. The templates are measured in Fig. 7 I(c). These are arranged in a lensless configuration  $\{d = 0.2\text{mm}; u = 5.2\text{mm}\}$ . While we optimized the design for a  $20^\circ$  eFOV, our detector only considers the centers of the nine template responses and does not angularly localize the face. It outputs a response using a linear classifier with no bias term (ensuring invariance to intensity scaling).

**Tracking targets:** Tracking, in its simplest form, can be implemented as sequential per-frame detection, and thus can be achieved optically using the sensors described above for face detection. If one can afford slightly more computation, then the classifiers used for detection can be combined with a dynamic model to improve performance (e.g., [3], [2]). In either case, we save computation by performing optical filtering-for-matching.

In Fig. 7 (VI), we show a detector with two templates, a “T” pattern  $\{d = 0.2\text{mm}; u = 3.7\text{mm}\}$  and a small cir-

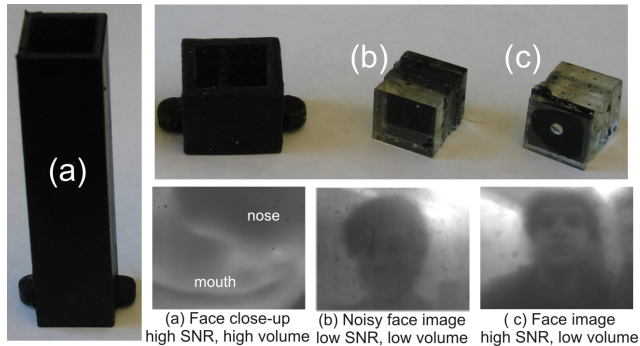


Figure 8. Three setups that integrate light over the same solid angle. (a) and (b) are pinholes of radii 2.5mm and 0.1mm, while (c) is an lenslet of radii 2.5mm embedded in acrylic plastic. Lenses collect more light, and hence the SNR advantage of (c) over (b). Additionally, the lenslet (b) allows a compact setup when compared to (a), as shown by the difference in holder size.

cle  $\{d = 0.1\text{mm}; u = 3.7\text{mm}\}$ , optimized for a  $90^\circ$  eFOV. After appropriate initialization, we track the target by finding, in a gated region of each subsequent frame, the image point where the pair of template responses is closest to the initial ones. The non-optical computation that is required is limited to a small number of subtractions and a minima calculation. We show tracking for an outdoor scene, with obstacles, over the whole field of view.

## 6. Discussion

Our analysis of optical designs assumes that a set of templates have been pre-chosen or pre-learned for the task at hand. Developing machine learning tools specifically for our platforms may be a worthwhile direction to pursue. These tools should account for fabrication constraints (e.g., resolution and bit-depth) and template distortion ( $\Delta$ ) during learning, and they should be capable of producing templates that not only have discriminative spatial patterns, but discriminative spectral responses as well. Indeed, the ability to easily specify a unique spectral profile (over UV, VIS, and NIR) for each template in our sensors may enhance their utility by endowing them with characteristics, such as lighting, pose, and scale insensitivity, typically associated with conventional vision systems.

Extending our work with a formal analysis of noise is also possible. While we briefly mention that lenslets improve the signal-to-noise ratio, this could be analyzed by specifying a sensor noise model and exploring the trade-offs between SNR, volume, mass, and field of view for various designs. Finally, this work is only one example of how optical processing can perform vision on a tight budget. We may consider using other optical elements, such as adaptive templates [28], artificial insect eyes [18], [17], CentEye chips (<http://www.centeye.com/>), curved sensors [20], [21], and multiplexed configurations [37], as and when they become widely available in small, low-power form factors.

## Appendix

**Lensless imaging:** In Fig. 9 (left),  $l_1 = l_2 = \|AB\| \frac{(v+u)}{u}$ ; the sensor convolves a stretched version of the template with a planar scene at a distance  $(v+u)$ . This is the scenario explained in [45]. However, for distant scenes defined on the hemisphere, the solid angles are important.  $\triangle ABP_1$  and  $\triangle ABP_2$  have the same base but different sides, and so the two angular supports are unequal;  $\omega_1 \neq \omega_2$ .

**Aperture thickness vignetting:** In Fig. 9 (right), total occlusion occurs when  $\arctan(\frac{t}{d}) = \arctan(\frac{u-t}{x-\frac{d}{2}})$ . If  $x < \frac{d}{2}$ , no vignetting occurs. Elsewhere, the angular support decreases by  $\omega_{vig} = \arccos(\frac{(y'+a)^2 + (a')^2 - (u-t)^2}{2(y'+a)(a')})^{0.5}$ , where  $y' = ((\frac{t(x-\frac{d}{2})^2 + u^2 t^2}{u^2}))^{0.5}$ ,  $a = (\frac{(u^2(u-t)^2 + (x-\frac{d}{2})u^2 - t(x-\frac{d}{2}))^2}{u^2})^{0.5}$  and  $a' = \frac{(4(u-t)^2 + (2x-d)^2)^{0.5}}{2}$ .

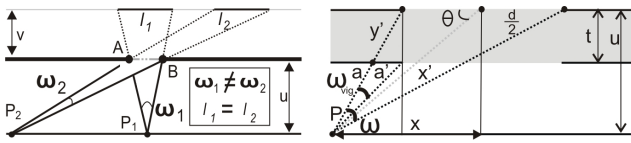


Figure 9. Lensless imaging and aperture vignetting

**Acknowledgements** The project was supported by an NSF award IIS-0926148, an ONR award N000140911022, and the US Army Research Laboratory and the US Army Research Office under contract/grant number 54262-CI.

## References

- [1] Zeemax optical software <http://www.zemax.com/>, 2010.
- [2] S. Avidan. Support vector tracking. *CVPR*, 2001.
- [3] M. J. Black and A. D. Jepson. Eigenttracking: robust matching and tracking of articulated objects using a view-based representation. *IJCV*, 1998.
- [4] N. Borrelli. Microoptics technology: fabrication and applications of lens arrays and devices. 1999.
- [5] V. Brajovic and T. Kanade. Computational sensor for visual tracking with attention. *Solid State Circuits*, 1998.
- [6] A. Chandrakasan, N. Verma, J. Kwong, D. Daly, N. Ickes, D. Finchelstein, and B. Calhoun. Micropower wireless sensors. *NSTI Nanotech*, 2006.
- [7] V. Chari and P. Sturm. Multi-view geometry of the refractive plane. *BMVC*, 2009.
- [8] Collection. Flying insects and robots. *Springer*, 2009.
- [9] A. Davenport, P. Boufounos, M. Wakin, and R. Baranuik. Signal processing with compressive measurements. *IEEE Journal of Selected Topics in Signal Processing*, 2009.
- [10] M. Edge and I. Turner. The underwater photographer. *Focal Press*, 1999.
- [11] J. H. Elder and S. W. Zucker. Local scale control for edge detection and blur estimation. *PAMI*, 1998.
- [12] C. Farabet, C. Poulet, and Y. LeCun. An FPGA-based stream processor for embedded real-time vision with convolutional networks. *ECV*, 2009.
- [13] A. Fluegel. <http://glassproperties.com/>. 2007.
- [14] J. W. Goodman. Introduction to fourier optics. *McGraw-Hill*, 1968.
- [15] B. Gyselinckx, C. Van Hoof, J. Ryckaert, R. Yazicioglu, P. Fiorini, and V. Leonov. Human++: autonomous wireless sensors for body area networks. In *Custom Integrated Circuits Conference, 2005. Proceedings of the IEEE 2005*, pages 13–19. IEEE, 2006.
- [16] H. P. Herzig. Micro-optics: Elements, systems and applications. 1999.
- [17] S. Hiura, A. Mohan, and R. Raskar. Krill-eye : Superposition compound eye for wide-angle imaging via grin lenses. *OMNIVIS*, 2009.
- [18] K. Jeong, J. Kim, and L. Lee. Biologically inspired artificial compound eyes. *Science*, 2006.
- [19] M. Karpelson, G. Wei, and R. J. Wood. Milligram-scale high-voltage power electronics for piezoelectric microrobots. *ICRA*, 2009.
- [20] H. Ko, G. Shin, S. Wang, M. Stoykovich, J. Lee, D. Kim, J. Ha, Y. Huang, K. Hwang, and J. Rogers. Curvilinear electronics formed using silicon membrane circuits and elastomeric transfer elements. *Small*, 2009.
- [21] G. Krishnan and S. K. Nayar. Towards a true spherical camera. *SPIE*, 2009.
- [22] N. Kumar, A. C. Berg, P. Belhumeur, and S. K. Nayar. Attribute and simile classifiers for face verification. *ICCV*, 2009.
- [23] Y. LeCun, L. Bottou, Y. Bengio, and P. Haffner. Gradient based learning applied to document recognition. *Proceedings of the IEEE*, 1998.
- [24] A. Levin, R. Fergus, and B. Freeman. Image and depth from a conventional camera with a coded aperture. *SIGGRAPH*, 2007.
- [25] D. Marr and E. Hildreth. Theory of edge detection. *Proceedings of the Royal Society of London*, 1980.
- [26] K. Mielenz. On the diffraction limit for lensless imaging. *Journal of Research of the NIST*, 1999.
- [27] K. Miyamoto. Fish eye lens. *JOSA*, 1964.
- [28] S. K. Nayar, V. Branzoi, and T. E. Boulton. Programmable Imaging: Towards a Flexible Camera. *IJCV*, 2006.
- [29] R. Ng. Fourier slice photography. *TOG*, 2005.
- [30] M. O'Toole and K. Kutulakos. Optical computing for fast light transport analysis. *SIGGRAPH Asia*, 2010.
- [31] F. Pedrotti and L. Pedrotti. Introduction to optics. 2006.
- [32] C. Raghavendra, K. Sivalingam, and T. Znati. Wireless sensor networks. *Springer*, 2004.
- [33] E. Steltz and R. Fearing. Dynamometer power output measurements of miniature piezoelectric actuators. *Transactions on Mechatronics*, 2009.
- [34] R. Swaminathan, M. Grossberg, and S. Nayar. Caustics of catadioptric cameras. *ICCV*, 2001.
- [35] J. Tanida, T. Kumagai, K. Yamada, S. Miyatake, K. Ishida, T. Morimoto, N. Kondou, D. Miyazaki, and Y. Ichioka. Thin observation module by bound optics (tombo): Concept and experimental verification. *Applied Optics*, 2001.
- [36] T. Treibitz, Y. Schechner, and H. Singh. Flat refractive geometry. *CVPR*, 2008.
- [37] S. Uttam, N. Goodman, M. Neifeld, C. Kim, R. John, J. Kim, and D. Brady. Optically multiplexed imaging with superposition space tracking. *Optics Express*, 2009.
- [38] A. Veeraraghavan, R. Raskar, A. Agrawal, A. Mohan, and J. Tumblin. Dappled photography: Mask enhanced cameras for heterodyned light fields and coded aperture refocusing. *SIGGRAPH*, 2007.
- [39] P. A. Viola and M. J. Jones. Robust real-time face detection. *IJCV*, 2004.
- [40] R. Volker, M. Eisner, and K. Weible. Miniaturized imaging systems. *Microelectronic Engineering*, 2003.
- [41] A. Wilhelm, B. Surgenor, and J. Pharoah. Evaluation of a micro fuel cell as applied to a mobile robot. *ICMA*, 2005.
- [42] W. Wolf, B. Ozer, and T. Lv. Smart cameras as embedded systems. *Computer*, 2002.
- [43] R. W. Wood. Physical optics. *Macmillan*, 1911.
- [44] F. Yu and S. Sutajumalia. Optical pattern recognition. *Cambridge University Press*, 1998.
- [45] A. Zomet and S. Nayar. Lensless imaging with a controllable aperture. *CVPR*, 2006.